Interaction of mean and oscillating plasma flows across confinement mode transitions

Garrard D. CONWAY, Emanuele POLI, Tim HAPPEL[1)]
and the ASDEX Upgrade Team

MPI Plasmaphysik, EURATOM-Association IPP, D-85748, Garching, Germany
[1)] *Laboratorio Nacional de Fusión, EURATOM-Association CIEMAT, 28040, Madrid, Spain*

February 18, 2010

The interaction of mean plasma flows (driven by equilibrium $E \times B$ forces) and oscillating plasma flows - such as zonal flows (ZFs) and geodesic acoustic modes (GAMs) - (radially localized $E \times B$ plasma flows generated by non-linear turbulence interactions) is investigated in the ASDEX Upgrade tokamak using Doppler reflectometry. ZFs and GAMs play an important role in magnetic confinement devices by enhancing the velocity shearing of turbulent eddies which reduces turbulent cross-field transport. Although the GAM is universally observed across the plasma edge gradient region of ohmic and additionally heated low confinement L-mode regimes, it is not seen in the high confinement H-mode. Using slow power ramping of the additional ECRH and NBI heating systems the behaviour of the edge GAM, and its interaction with the mean flow shear, i.e. the radial electric field E_r profile, across the L to H-mode transition are studied. As the edge E_r well deepens with improving confinement, the associated negative E_r shear region narrows and the radial extent of the GAM shrinks. The main feature, however, is the movement of spectral power out of the coherent GAM into large amplitude, low frequency random flow perturbations. It is speculated that these flow perturbations may play a role in the triggering of the confinement transition.

Keywords: Turbulence, GAMs, H-mode transition, Doppler reflectometry

DOI: 10.1585/pfr.5.000

1. Introduction

Zonal flows (ZFs) and their oscillating counterpart, geodesic acoustic modes (GAMs), are radially localized $E \times B$ plasma flows generated by non-linear turbulence interactions [1]. In magnetic confinement devices, such as tokamaks and stellarators, ZFs are believed to play an important role in reducing turbulent transport by enhancing the velocity shearing of turbulent eddies [2]. Numerical simulations of core tokamak turbulence indeed show that the inclusion of the zonal flow component is necessary in order to reduce the simulated turbulence correlation lengths down to experimentally measured values [3]. The ZF is an additional player in the widely accepted model of turbulence suppression by sheared flow [4]. Here, a stable *mean* flow shear (e.g. the $E \times B$ shear driven by the plasma gradients and momentum input) decorrelates the turbulent eddy structures when the shear rate exceeds the natural eddy turn-over rate, which reduces cross-field transport, and in-turn leads to enhanced profile gradients and thus stronger edge E_r shear etc. - a positive feedback loop, which has been used to explain the formation of transport barriers. Of course the increased profile gradients may also drive the turbulence harder, so, for an equilibrium energy flow the gradients will adjust to values which support the turbulence level and commensurate shearing action and transport. To trigger a confinement mode bifurcation, such as the H-mode, requires some additional enhancement of one of the feedback loop components - such as enhanced shearing due to turbulence induced ZFs/GAMs etc. - to push the system to a new equilibrium level.

In the high gradient plasma edge region the ZF is damped and supplanted by the GAM [1]. The shearing action of the oscillating GAM maybe thought to be less effective than that of the 'static' or quasi-zero frequency ZF, however, its frequency (typically $5 - 25\,\mathrm{kHz}$) is still substantially lower than the turbulent eddy turn-over frequency and its poloidal displacement amplitude (several mm) is large or comparable to the turbulence structure size, i.e. poloidal and radial correlation lengths [5]. In addition, the GAM provides an additional energy dissipation route for the turbulence via Landau and collisional damping. Thus, the GAM is expected to have an equivalent important role in moderating the edge turbulence behaviour [1].

GAMs are universally observed in ohmic and additionally heated low confinement L-mode regimes [see ref. [6] for a recent review of measurements], however, they have not to-date been seen in the high confinement H-mode [7]. What happens to the GAM across the L to H-mode transition, and what role it might play in the self-suppression of the edge turbulence in the H-mode, or indeed in triggering the transition through enhanced eddy shearing, and its interaction with the mean shear flow are still open issues [8] - and the topic of this paper.

author's e-mail: Garrard.Conway@ipp.mpg.de

ZFs and GAMs are flow perturbations and hence their measurement presents a particular challenge. In low temperature plasmas Langmuir probes have been employed to measure coherent potential fluctuations, however, in the more relevant hot plasma confinement devices non-invasive diagnostic techniques such as Heavy ion beam probes (HIBP) and beam emission spectroscopy (BES) are required - see ref. [6] for an overview. Microwave Doppler reflectometry has also become an important diagnostic technique in recent years, with systems either routinely operating or under active development on a growing number of fusion devices. The attractiveness of Doppler reflectometry is its high spatial and temporal resolution of the $E \times B$ velocity profile, the radial electric field, E_r and its fluctuations. This last feature has been used extensively to investigate the behaviour of edge and core GAMs in the ASDEX Upgrade tokamak (AUG) [5, 7, 9].

In the following sections the Doppler reflectometry principle is described, including the latest analysis techniques used on AUG. The behaviour of the mean E_r profile through the various tokamak confinement regimes is presented, followed by a review of recent results on the edge GAM behaviour, then finally new results on the behaviour of the GAM across the L to H-mode transition and the interplay with the mean E_r shear are presented.

2. Doppler reflectometry technique

Doppler reflectometry (also called Doppler backscatter) is a hybrid diagnostic technique which combines the turbulence wavenumber selectivity of coherent scattering and the radial localization of microwave / mm-wave reflectometry. By deliberately tilting a standard fluctuation reflectometer (in the tokamak poloidal plane) so as to make an angle to the plasma density gradient ∇n_e the launched beam is refracted as it propagates into the plasma - shown schematically in fig. 1. As the beam propagates up the density gradient its wavenumber decreases with the squared refractive index, $k_i^2 = N^2 k_o^2$ (where $N^2 = N_\perp^2 + N_\parallel^2$), until it reaches a minimum - the cutoff condition coinciding where the beam is turned and reflected back out of the plasma. For a plane or flat cutoff layer this occurs at $N^2 = \sin^2\theta_o$ where θ_o is the beam incident angle at the plasma boundary [10]. (For normal incidence $N^2 \to 0$.)

At the turning point the beam is propagating parallel to the cutoff layer and is sensitive to N^2 fluctuations - i.e. density fluctuations - which scatter the beam. If the density fluctuation spectrum contains wavenumbers satisfying the Bragg condition for the beam wavevector at the turning point, $\boldsymbol{k} = -2\boldsymbol{k_i} = -2\boldsymbol{N}k_o$ (for the monostatic antenna configuration of fig. 1) then radiation will be scattered back to the reflectometer receiver antenna [11, 12]. If the fluctuations move relative to the diagnostic antennas the backscattered signal spectrum is Doppler frequency shifted by $2\pi f_\mathrm{D} = \omega_\mathrm{D} = \boldsymbol{u}\cdot\boldsymbol{k} = u_\perp k_\perp + u_\parallel k_\parallel + u_\mathrm{r}k_\mathrm{r}$, where $\boldsymbol{u}$ is the mean velocity of the density fluctuations

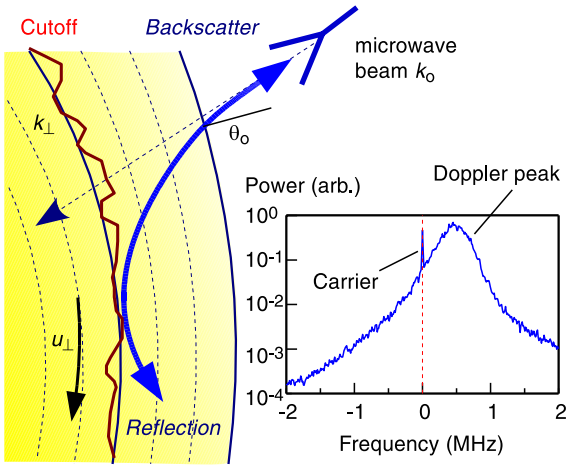

Fig. 1 Schematic showing the Doppler reflectometry measurement principle and a typical ohmic Doppler spectrum.

and $\boldsymbol{k}$ the Bragg matched wavenumber. Fig. 1 shows a typical Doppler spectrum, from the edge region of an ohmic AUG discharge, with the carrier wave spike at zero frequency and a Doppler shifted peak on a background noise floor.

Both the radial and parallel components of the Doppler shift can be neglected, i.e. $\omega_\mathrm{D} \approx u_\perp k_\perp$. Broadband turbulence usually has a symmetric zero-centred radial k_r spectrum and u_r velocity distribution - i.e. balanced inward and outward movement - which broadens the reflectometer spectrum without contributing to the Doppler shift. Radially propagating disturbances, such as density 'blobs' and filaments expected in the edge/SOL region, may still generate Doppler shifts. Conversely, the parallel component is asymmetric, but fortunately small. Tokamak turbulence is generally drift-wave like in nature with parallel wavenumbers scaling inversely with the field line connection length, i.e. $k_\parallel \sim 1/qR_o \sim 0.005\,\mathrm{cm}^{-1}$ for $R_o \sim 2$ m and $q > 1$, which is orders of magnitude smaller than typical probed $k_\perp$ values of $5 - 15\,\mathrm{cm}^{-1}$.

As the probing microwave wavelength is large compared to the Debye length the scattering is essentially due to the gyrocentre motion of the turbulence, i.e. the Doppler shift is directly proportional to the phase velocity of the fluctuations v_ph moving in the plasma $E \times B$ (guiding centre) frame, $u_\perp = v_{E\times B} + v_\mathrm{ph}$. If v_ph is known, or small $v_{E\times B} \gg v_\mathrm{ph}$, then the $E \times B$ velocity, and hence the radial electric field E_r, can be extracted directly from ω_D with good accuracy [12–14]. The magnitude of v_ph has been investigated using linear and non-linear gyrokinetic turbulence codes for realistic tokamak conditions [15]. In both the steep edge gradient region (dominant toroidal electron drift wave EDW turbulence) and shallower core gradient region (Ion-temperature gradient ITG or trapped electron mode TEM turbulence) phase velocities much smaller than the diamagnetic drift velocity, $v^* = \rho_\mathrm{s} c_\mathrm{s}/L_n$, are obtained (also confirmed by experimental core measurements [16]

and HIBP comparisons [17]). Typically $v_{\rm ph} \approx 3\rho_{\rm s}c_{\rm s}/R$ (where $\rho_{\rm s} = c_{\rm s}/\omega_{ci}$) for $k_\theta\rho_{\rm s} < 0.6$, which for H-mode parameters is only a few hundred m s^{-1} and thus may be neglected compared to typical $u_\perp$ of several km s^{-1}.

The backscattered power is proportional to the turbulence spectral power $S(k_\perp,\omega) = |\delta n(k_\perp,\omega)|^2$ at the probed $k_\perp$. Thus the turbulence spectrum can be measured simply by scanning the tilt angle θ_o to vary the probed $k_\perp$ [12, 18, 19]. Also, since $E_{\rm r}$ fluctuations $\delta E_{\rm r}$ translate directly to $\delta v_{E\times B}$ which in turn appear as $\delta f_{\rm D}$, this allows direct access to long wavelength $E_{\rm r}$ flow oscillations such as GAMs and zonal flows [7].

For $u_\perp$ measurements, where the turbulence is simply used as a tracer to generate the backscatter, a sufficient turbulence amplitude is an essential requirement to create a measurable Doppler peak above the diagnostic noise floor, or any direct reflection component in the spectrum. Since the turbulence k-spectrum typically peaks around $k_\perp\rho_{\rm s} \sim 0.3$ and decays with a spectral index $n \approx -3$ this defines the usable range of antenna tilt angles. The Bragg condition $k_\perp = mk \approx 2k_o\sin\theta$ means higher m orders will also appear at the same Doppler frequency for any fixed tilt angle. Where the turbulence is used purely as a tracer this is a positive effect which extends operational range of tilt angles. But, if the aim is to measure the k-spectrum then this may create ambiguity in the probed k and distortion in the measured spectrum.

The diagnostic k resolution scales inversely with the beam radius $\Delta k \propto 2\sqrt{2}/w$ (for a flat cutoff), and a localization Δr scaling roughly with the Airy lobe width and the decay length of the evanescent electric field pattern around the cutoff. Cutoff layer curvature and beam divergence will increase the spread in the probed k_i and hence reduce the localization and resolution [20]. Thus, the optimal antenna is a low *poloidal* divergence Gaussian beam with a large diameter and a phase front matched to cutoff curvature. For the more typical focused horn antennas attention must be paid to the antenna side-lobes, which can, if the main lobe signal is poor - c.f. weak turbulence, core probing or high $k_\perp$ - allow additional Doppler peaks to enter [15].

3. AUG Doppler systems

Fig. 2 shows the layout of the Doppler reflectometers on AUG. Three systems are currently in operation: two V-band ($50-75$ GHz), one in O-mode and one in X-mode polarization, plus a W-band ($75-108$ GHz) in either O or X-mode polarization. Probing is from the tokamak low-field-side; the V-band in toroidal sector 13 using fixed antenna lines-of-sight, above and below the poloidal mid-plane, and the W-band in sector 5 with a remote steerable mirror around the mid-plane to vary the angle θ_o [19]. Adjacent antennae launch and collect the scattered signal, which is down-converted using a heterodyne receiver with in-phase and quadrature detection. The complex amplitude signals ($I + iQ = Ae^{i\phi}$) are sampled at 20 MHz in 12-bit for up to 8 s [14].

The measurement position can be scanned in $50-200$ ms by stepping the microwave probe frequency staircase fashion to give a radial profile. The profile repetition period is set by the desired radial resolution (number of steps, typically > 20) and the Doppler frequency resolution (step length: $3-20$ ms). For flat cutoff layers $N_\perp \approx \sin\theta_o$, but in practice each measurement position (beam turning point), $k_\perp = 2N_\perp k_o$ and $k_\parallel = 2N_\parallel k_o$ are obtained using the TORBEAM beam tracing code [21] with fitted experimental density profiles using DCN interferometry, Thomson scattering, Lithium beam and FM profile reflectometry data, and equilibrium reconstructions from the CLISTE code.

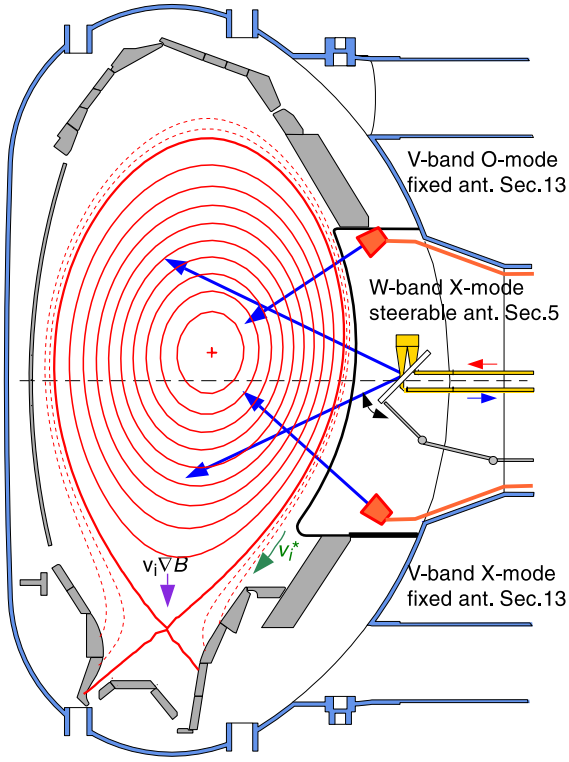

Fig. 2 AUG poloidal cross-section showing layout of Doppler reflectometer antennas.

The antennas are also tilted toroidally by a few degrees ($\phi_o \approx +2^\circ$ [X] & -3° [O-mode]) so that the beam meets the B field close to perpendicular. The requirement is to minimize the beam $k_\parallel$ at the turning point so as to satisfy the Bragg requirement for a narrow $S(k_\parallel)$ turbulence spectrum. However, as the B field inclination/helicity varies with the q and radial position it is not possible to optimize for all conditions. Fortunately the *toroidal* beam divergence ensures the Bragg condition is met somewhere across the beam, but with a reduced return signal [11].

The mean Doppler frequency is obtained by a Gaussian curve fit to the asymmetric component of the complex amplitude spectra. The fluctuating component is obtained by sliding an FFT window through the I and Q signals to

generate a sequence of spectra from which a time series of the Doppler shift $f_{\rm D}$ and integrated spectral amplitude $\mathcal{A}$ (fluctuations in $|\delta n_{\rm e}|^2$ at the probed $k_\perp$) are created. Further Fourier analysis then reveals the GAM behaviour.

4. Mean flow & $E_{\rm r}$ profiles

Fig. 3 shows radial electric field $E_{\rm r} = -v_{E\times B} \cdot B$ profiles across the plasma edge for a typical -2 T, $+0.8$ MA ELMy H-mode AUG discharge (#18676) with NBI heating. The profiles were obtained using the dual channel O and X-mode polarization V-band Doppler system and the fixed poloidally tilted antenna pairs on the tokamak low-field-side.

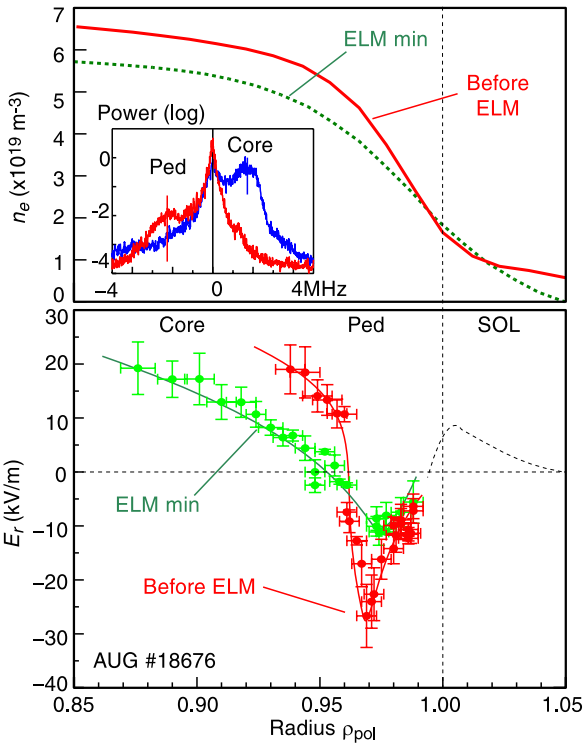

Fig. 3 $E_{\rm r}$ and $n_{\rm e}$ profiles for H-mode #18676 showing the profile collapse after an ELM.

In the tokamak scrape-off-layer (SOL) the mean $v_{E\times B}$ velocity always flows in the ion drift direction (i.e. positive $E_{\rm r}$) but reverses across the separatrix (electron direction) due to the strong pedestal pressure gradient and poloidal fluid velocity to form a deep negative edge $E_{\rm r}$ well [14]. The $E_{\rm r}$ well is generally located around the region of maximum pressure gradient ∇P, which is typically in the upper half of the pedestal region as shown by the corresponding density profiles. Inside the pedestal top, towards the core, the $E_{\rm r}$ / flow can remain negative or reverse to positive depending on the presence of core momentum injection from the NBI heating sources etc. The edge negative $E_{\rm r}$ well depth scales with the energy confinement. Typically $E_{\rm r}$ of -3 to $-6\,{\rm kV\,m^{-1}}$ are observed for ohmic and and NBI L-mode conditions, increasing to $-15\,{\rm kV\,m^{-1}}$ for improved confinement L-modes, and finally rising from -25 to $-50\,{\rm kV\,m^{-1}}$ for well developed H-modes [22].

The edge $E_{\rm r}$ well forms two shear regions - radial gradients $\partial E_{\rm r}/\partial r$ - an outer positive shear associated with the separatrix and SOL flows, and an inner negative shear associated with the upper pedestal gradient. The positive shear often grows first as the H-mode begins to form from the L-mode with the $E_{\rm r}$ well moving outward, then the negative shear rises quickly around and after the actual L-H transition with the $E_{\rm r}$ well deepening and moving inward [23] - i.e. the strong negative shear region narrows radially. This narrowing and inward movement of the well is also observed in the improved confinement L-modes, but without the classic edge turbulence reduction.

Two $E_{\rm r}$ profiles are shown in fig. 3: before and during an ELM. The data are synchronized to several ELMs over a 300 ms period. During the ELM phase the $E_{\rm r}$ well collapses - in concert with the density profile - towards L-mode values with a corresponding outward well movement and a reduced and wider negative $E_{\rm r}$ shear region.

5. Oscillating flows - GAMs & ZFs

The parameter dependence of GAMs has been extensively studied on AUG [5, 7, 9]. They are ubiquitously seen in the edge region of ohmic and L-mode shots, but not in H-modes. Basically, ZFs exist only on closed field lines, i.e. inside the plasma separatrix. Fig. 4 shows the radial variation of the GAM for a -2.4 T, 0.4 MA, low density $\bar{n}_{\rm e} = 1.8 \times 10^{19}\,{\rm m^{-3}}$, 0.8 MW ECR heated, L-mode discharge. The GAM extends across the negative $E_{\rm r}$ shear region, and, as the $E_{\rm r}$ minimum is generally aligned with maximum ∇P the GAM begins towards the pedestal top, where it is also strongest. In this diverted X-point discharge the GAM extends in to a normalized radius $\rho_{\rm pol} = 0.8$ as $q_{95} \sim 9$ is very high and consequently the damping $\propto \exp(-q^2)$ is weak. Lower q_{95} discharges show the GAM constrained more to the density pedestal top. So far, there is no convincing evidence of any low frequency zonal flow activity inside of the pedestal top radius.

Fig. 4 shows the broadband RMS $u_\perp$ flow fluctuations, $\sigma(u_\perp)$, peaking at the separatrix and then decaying steadily across the GAM region. Towards the core $\sigma(u_\perp)$ rises sharply again, coinciding with the disappearance of the GAM. Note also in the $\mathcal{A}$ spectra of fig. 4 the decay in the density fluctuation modulation with decreasing radius.

The GAM frequency scales as $\omega = Gc_{\rm s}/R_o$ (sound speed over major radius) with a scale factor $G \approx \sqrt{2}$ in the core region of circular shaped limiter plasmas, i.e. elongation $\kappa \sim 1$ (in agreement with current theory and simulations). However, in the edge gradient region, where the the GAM is stronger, G is anomalous with an inverse dependence on κ [9, 24]. Likewise the edge GAM amplitude depends on the plasma equilibrium - increasing with the edge safety factor q (reduced damping) and decreasing with κ

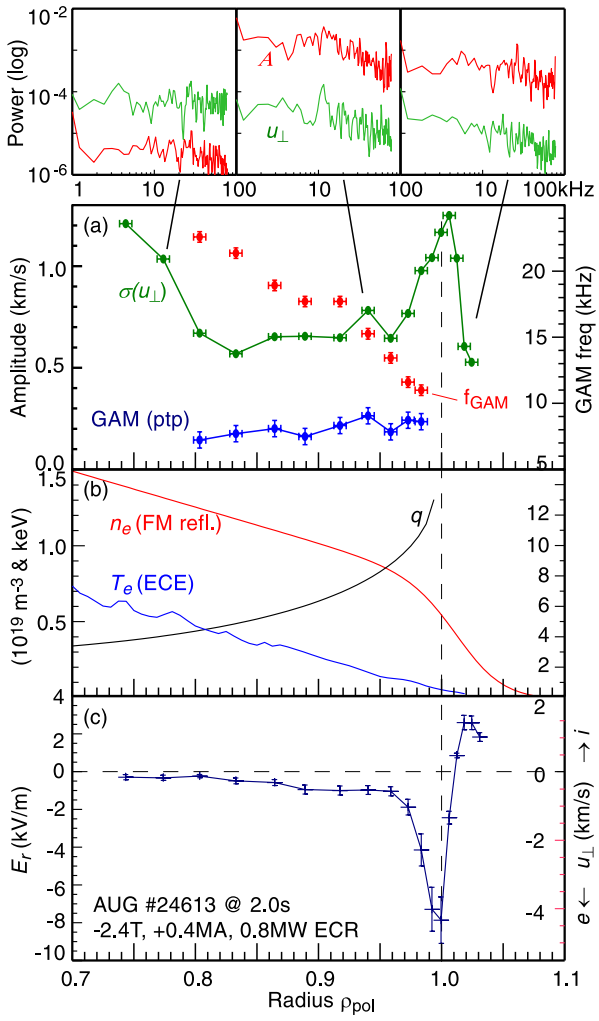

Fig. 4 Radial profiles of (a) GAM p.t.p. amplitude, GAM frequency and RMS flow $\sigma(u_\perp)$, (b) n_e, T_e and q, (c) E_r / $u_\perp$, plus selected flow $u_\perp$ and density $\mathcal{A}$ spectra for low density and high $q_{95} \sim 9$ shot #24613.

(increasing magnetic shear). Radially the GAM forms a set of nested zones with GAM frequency plateaus and steps at zonal boundaries. Generally, for diverted elongated plasmas only one zone is visible. The $m = \pm 1$ pressure (density) sideband mode is generally not seen as the Doppler measurements are close to the tokamak mid-plane. However, HIBP measurements show the GAM flow oscillation is well correlated in both the toroidal and poloidal directions, confirming the $m = n = 0$ mode structure, with a finite radial (zonal) extent, e.g. $k_r \neq 0$ [25–27].

The impact of the turbulence drive on the GAM is clearly seen with the GAM peak-to-peak amplitude $A_{\rm GAM}$ increasing linearly with the normalized temperature gradient $\nabla T_e / \sqrt{\kappa}$ - accompanied by the GAM radial maxima moving outward (towards higher q and lower damping) and a rising GAM frequency [5]. The (radial) mean GAM amplitude $\langle A_{\rm GAM} \rangle$ is roughly correlated with the energy confinement factor $H_{98} = \tau_{\rm E(exp)} / \tau_{\rm E(scale)}$, as shown in fig. 5, up to the L to H-mode transition.

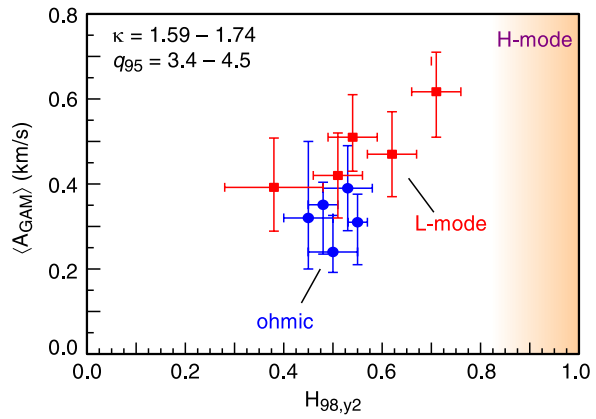

Fig. 5 Mean GAM peak-to-peak amplitude vs energy confinement factor $H_{98,y2}$ (ITER ELMy H-mode 98P scaling).

6. GAMs across the L-H transition

Using a combination of ECRH and increasing neutral beam heating a gradual transition into the H-mode can be engineered. Fig. 6 shows the evolution of the flow $u_\perp$ and density $\mathcal{A}$ fluctuation spectra (around the GAM maxima) with increasing heating power and confinement factor H_{98} during a $2.8 \times 10^{19}\,\mathrm{m}^{-3}$, $-2.5\,\mathrm{T}$, $+1.0\,\mathrm{MA}$, $q_{95} \sim 4$ shot #24750 with 1.4 MW of ECRH. A strong GAM is observed across the edge gradient region in the L-mode phase, but becomes distinctly narrower as the discharge enters an intermediate improved confinement state with increasing power. This reduction in the GAM radial extent is commensurate with a shrinking of the negative E_r shear region as the E_r well moves inward and deepens (e.g. increasing mean $E \times B$ flow velocity) in this discharge.

Both the GAM frequency and its amplitude, tend to rise as the H-mode transition is approached. Across the whole gradient region there is a significant increase in the level of both broadband background $u_\perp$ flow and density fluctuation modulation.

Once a fully developed H-mode forms, two things happen: the density turbulence drops across the pedestal region, and the GAM disappears into the rising level of background flow fluctuations, i.e. the $u_\perp$ spectral power moves out of the coherent GAM into increasing low frequency random flow fluctuations.

7. Discussion

There are two main conclusions that can be drawn from the results presented above:

(1) There is a link between the GAM (kHz flow oscillation) behaviour and the mean $E \times B$ flow - particularly the mean flow shear - both in terms of the GAM radial extent coinciding with the negative flow shear region; and the correlation between the GAM amplitude and the flow strength / E_r well depth and the energy confinement factor. As L-H transition is approached the radial extent over which the GAM exists narrows with the increasing flow

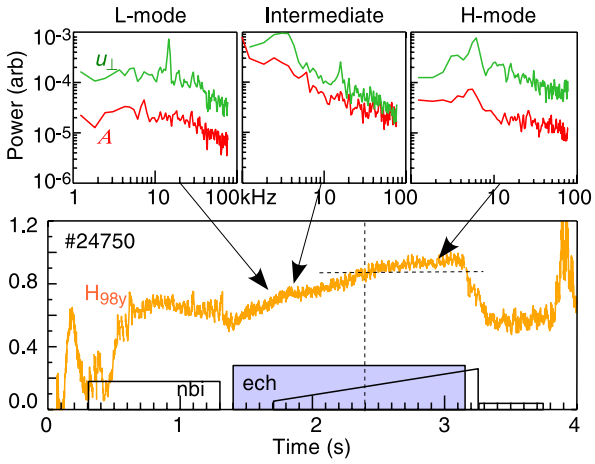

Fig. 6 Flow velocity $u_\perp$ and density $\mathcal{A}$ spectra during L-mode, Intermediate and H-mode phases of #24750 with increasing energy confinement factor H_{98}.

strength / E_r well, i.e. the flow oscillation k_r increases as it becomes more concentrated in a narrower spatial region.

(2) The flow oscillation power moves between the GAM and the broadband background fluctuations. Around the L-H transition the power shifts out of the coherent GAM into large amplitude random fluctuations. It is to be expected that an enhancement of low frequency flow oscillations should be more effective in decorrelating the turbulent eddies. It is tempting to speculate that the enhanced turbulence shearing due to these flow fluctuations may offer the much sought trigger to initiate the subsequent $E \times B$ velocity shear positive feedback loop which drives the bifurcation of the edge transport barrier in to the H-mode.

Although the GAM is clearly driven by the density turbulence (e.g. the scaling of the GAM amplitude with ∇T_e), and, it has a large physical peak-to-peak displacement comparable to the turbulence structure size close to the L-H transition, the relative causality (i.e. which changes first) between the GAM amplitude and the turbulence amplitude remains to be clarified.

Acknowledgments

We thank C. Tröster, W.Suttrop, J.Schirmer, J.Friesen and E.Schmidt for assistance with the diagnostic hardware, J.Vicente (IPFN) for reflectometer density profile validation, P.Sauter and F.Ryter for discussions on H-mode transitions and B.Scott & K.Hallatschek for discussions on GAMs.

[1] K.Itoh *et al.*, Phys. Plasmas **13**, 055502 (2006).
[2] T.S.Hahm *et al.*, Phys. Plasmas **6**, 922 (1999).
[3] T.L.Rhodes *et al.*, Phys. Plasmas **9**, 2141 (2002).
[4] P.W.Terry, Rev. Mod. Phys. **72**, 109 (2000).
[5] G.D.Conway and AUG Team, Plasma Phys. Control. Fusion **50**, 085005 (2008).
[6] A.Fujisawa, Nucl. Fusion **49**, 013001 (2009).
[7] G.D.Conway *et al.*, Plasma Phys. Control. Fusion **47**, 1165 (2005).
[8] G.D.Conway, Plasma Phys. Control. Fusion **50**, 124026 (2008).
[9] G.D.Conway *et al.*, Plasma Phys. Control. Fusion **50**, 055009 (2008).
[10] V.L.Ginzburg, *Propagation of Electromagnetic Waves in Plasma* (Gordon & Breach, New York, 1961).
[11] C.Honné *et al.*, Nucl. Fusion **46**, S809 (2006).
[12] P.Hennequin *et al.*, Nucl. Fusion **46**, S771 (2006).
[13] M.Hirsch *et al.*, Plasma Phys. Control. Fusion **43**, 1641 (2001).
[14] G.D.Conway *et al.*, Plasma Phys. Control. Fusion **46**, 951 (2004).
[15] G.D.Conway *et al.*, Proc. 8th Intl. Reflectometry Workshop for Fusion Plasma Diagnostics - IRW8 (St.Petersburg), http://plasma.ioffe.ru/irw8, pp30-36 (2007).
[16] G.D.Conway *et al.*, Nucl. Fusion **46**, S799 (2006).
[17] T.Estrada *et al.*, Plasma Phys. Control. Fusion **51**, 124015 (2009).
[18] C.Tröster *et al.*, Proc. 8th Intl. Refl. Wrks. - IRW8 (St.Petersburg), pp80-84 (2007).
[19] C.Tröster, Ph.D. Thesis, Ludwig-Maximilian University, Munich (2008).
[20] M.Hirsch and E.Holzhauer, Plasma Phys. Control. Fusion **46**, 593 (2004).
[21] E.Poli *et al.*, Comput. Phys. Commun. **136**, 90 (2001).
[22] J.Schirmer *et al.*, Nucl. Fusion **46**, S780 (2006).
[23] S.Klenge, *Dynamik magnetisch eingeschlossener Plasmen am L-H Übergang* Ph.D. Thesis, Univ. of Stuttgart, ISBN 3-933893-36-4 (Sierke Verlag, Göttingen, 2005).
[24] G.R.McKee *et al.*, Plasma Phys. Control. Fusion **48**, S123 (2006).
[25] T.Ido *et al.*, Nucl. Fusion **46**, 512 (2006).
[26] A.V.Melnikov *et al.*, Plasma Phys. Control. Fusion **48**, S87 (2006).
[27] A.Krämer-Flecken *et al.*, Plasma Phys. Control. Fusion **51**, 015001 (2009).